

# DualTSR: Unified Dual-Diffusion Transformer for Scene Text Image Super-Resolution

Axi Niu<sup>1</sup> Kang Zhang<sup>2</sup> Qingsen Yan<sup>1</sup> Hao Jin<sup>1</sup> Jinqiu Sun<sup>1</sup> Yanning Zhang<sup>1</sup>

<sup>1</sup>Northwestern Polytechnical University

<sup>2</sup>Korea Advanced Institute of Science and Technology

{nax, qingsenyan, sunjinqiu, ynzhang}@nwpu.edu.cn

jinh@mail.nwpu.edu.cn, zhangkang@kaist.ac.kr

## Abstract

*Scene Text Image Super-Resolution (STISR) aims to restore high-resolution details in low-resolution text images, which is crucial for both human readability and machine recognition. Existing methods, however, often depend on external Optical Character Recognition (OCR) models for textual priors or rely on complex multi-component architectures that are difficult to train and reproduce. In this paper, we introduce DualTSR, a unified end-to-end framework that addresses both issues. DualTSR employs a single multimodal transformer backbone trained with a dual diffusion objective. It simultaneously models the continuous distribution of high-resolution images via Conditional Flow Matching and the discrete distribution of textual content via discrete diffusion. This shared design enables visual and textual information to interact at every layer, allowing the model to infer text priors internally instead of relying on an external OCR module. Compared with prior multi-branch diffusion systems, DualTSR offers a simpler end-to-end formulation with fewer hand-crafted components. Experiments on synthetic Chinese benchmarks and a curated real-world evaluation protocol show that DualTSR achieves strong perceptual quality and text fidelity.*

## 1. Introduction

Scene Text Image Super-Resolution (STISR) aims to reconstruct high-quality scene text images from low-resolution inputs. The task is especially challenging because character structures are sensitive to degradation: small distortions, missing strokes, or blending with background clutter can alter the underlying semantics. Unlike general image super-resolution, which primarily enhances textures, STISR must simultaneously guarantee *textual fidelity* and *stylistic realism*. Any structural error directly causes recognition failure, while inconsistencies in font, color, or orientation reduce vi-

sual plausibility. These difficulties are further amplified in languages with large character sets such as Chinese.

To reduce the inherent ambiguity of STISR, recent work [2, 24, 25, 36] incorporates textual priors extracted from a pre-trained OCR model. Knowing the expected text sequence significantly constrains the solution space and often improves reconstruction quality. This OCR-guided paradigm has therefore become dominant, and several recent methods [29, 44] explicitly condition the SR process on predicted text tokens to enforce semantic correctness. However, its reliability is fundamentally limited by the accuracy of the external OCR: erroneous predictions propagate into the SR network, leading to hallucinated strokes, incorrect glyphs, and overall degraded results. To mitigate this dependency, subsequent works introduced stronger low-level priors. MARCONet [13] learns a discrete codebook of character structures to provide robust structural guidance, while GlyphSR [39] goes further by generating explicit glyph masks using SAM to supervise fine-grained stroke reconstruction. Although these structural priors alleviate the brittleness of OCR guidance, they require increasingly complex and multi-stage pipelines for prior extraction. This growing reliance on external modules highlights a core limitation of existing approaches and motivates a unified framework that can learn both semantic and structural cues internally without handcrafted or externally produced priors.

To this end, diffusion-based generative models [17, 33] have recently been adopted for STISR, particularly for complex scripts [29, 44]. DiffTSR [44] reports strong results by modeling text and image with separate modules connected through a multi-modality fusion block. While effective, this multi-stage architecture is cumbersome: it increases system size, complicates training, and limits the depth of cross-modal interaction because textual and visual information are only exchanged at specific fusion points.

To address the reliance on external OCRs and the complexity of multi-module designs, we propose DualTSR,

an end-to-end STISR framework built upon a single multi-modal transformer. `DualTSR` unifies super-resolution and text recognition within a dual diffusion objective: a Conditional Flow Matching model generates the high-resolution image, while a discrete diffusion model predicts the character sequence. These two processes operate within a shared architecture, enabling the model to infer its own text priors directly from visual cues and to exploit bidirectional interactions between the evolving text and image representations. This yields a single-model, deeply fused alternative to prior modular pipelines.

Our contributions are threefold:

- We present `DualTSR`, a unified STISR framework that jointly learns image super-resolution and text recognition within a single multimodal transformer.
- We design a dual diffusion objective, continuous (flow matching) for images and discrete diffusion for text, that removes the need for external OCR priors and avoids complex multi-stage architectures.
- Experiments on synthetic Chinese benchmarks and a curated real-world evaluation protocol show that `DualTSR` delivers strong perceptual quality and text reconstruction accuracy while preserving a unified end-to-end design.

## 2. Related Work

### 2.1. Text Image Super-Resolution

Research in Text Image Super-Resolution (TISR) addresses the unique challenges of simultaneously enhancing image details and improving text legibility. While general-purpose blind super-resolution methods such as BSRGAN [40] and Real-ESRGAN [38] restore natural images well, they often fail to preserve the fine-grained structures and appearance cues required for text. This has motivated specialized STISR methods that introduce text-specific priors or auxiliary supervision.

Early and mid-stage STISR work explored complementary cues for restoration. Text Gestalt [3] emphasizes stroke-aware reconstruction, TATT [23] introduces text attention to improve robustness to spatial deformation, and C3-STISR [45] combines multiple clues to recover both semantics and structure. A large line of work then adopts OCR-guided priors, where a pre-trained recognizer predicts text that is fed into the SR network to enforce semantic correctness [24, 29, 36, 44]. These methods can substantially improve recognition-oriented metrics, but their performance remains tied to the quality of the external OCR prior.

More recent methods instead emphasize structural priors. MARCONet [13] learns a character-structure codebook, MARCONet++ [14] further strengthens this line with improved character priors, and GlyphSR [39] uses explicit glyph masks generated from an auxiliary pipeline. These

approaches reduce dependence on raw OCR predictions, but they also introduce additional stages, modules, or prior-generation procedures. Our method differs from both families: rather than injecting a separately predicted text prior or a handcrafted structural prior, **DualTSR** learns image restoration and text prediction jointly within one multi-modal backbone.

### 2.2. Diffusion Models in Super-Resolution

Diffusion probabilistic models have demonstrated state-of-the-art performance in image synthesis and restoration, owing to their powerful ability to model complex data distributions [10, 17]. This success has naturally led to their application in both natural image super-resolution [27, 28, 31] and TISR [19, 46, 48]. Furthermore, research has shown that diffusion models are not only suitable for continuous data like images but can also effectively model discrete data distributions, such as text sequences [1, 21, 26, 30].

In the context of TISR, diffusion models have been used in several ways to mitigate unreliable priors and ambiguous degradations. PEAN [46] refines text-aware features with diffusion-based priors, TextDiff [18] uses mask-guided residual diffusion for restoration, and recognition-guided or text-conditional diffusion models [29, 48] strengthen the coupling between restoration and text prediction. DiffTSR [44] further separates image generation and text generation into dedicated diffusion branches connected by a multi-modality module, which is particularly effective for Chinese scene text. In contrast, **DualTSR** uses a single multimodal transformer with two coupled objectives: flow matching for the image branch and discrete diffusion for the text branch. This design keeps the joint modeling ability of diffusion-based STISR while reducing dependence on multiple specialized sub-networks and explicit cross-model fusion modules.

## 3. Method

We introduce **DualTSR**, an end-to-end multi-modal diffusion framework for scene text image super-resolution. Our approach utilizes a unified backbone to jointly model the distribution of high-resolution images and their corresponding textual content. Given a low-resolution input image  $\mathbf{x}^{\text{lr}}$ , our objective is to model the conditional distribution  $p(\mathbf{x}^{\text{hr}}, \mathbf{x}^{\text{txt}} | \mathbf{x}^{\text{lr}})$ , enabling the simultaneous generation of a high-resolution image  $\mathbf{x}^{\text{hr}}$  and its embedded text  $\mathbf{x}^{\text{txt}}$ . As illustrated in Figure 1, the `DualTSR` architecture comprises three core components: (1) a conditional flow matching model for high-resolution image synthesis  $p(\mathbf{x}^{\text{hr}} | \mathbf{x}^{\text{lr}}, \mathbf{x}^{\text{txt}})$ ; (2) a discrete diffusion model for optical character recognition (OCR) text generation  $p(\mathbf{x}^{\text{txt}} | \mathbf{x}^{\text{lr}}, \mathbf{x}^{\text{hr}})$ ; and (3) a multi-modal transformer that unifies these processes to learn the joint distribution  $p(\mathbf{x}^{\text{hr}}, \mathbf{x}^{\text{txt}} | \mathbf{x}^{\text{lr}})$ .

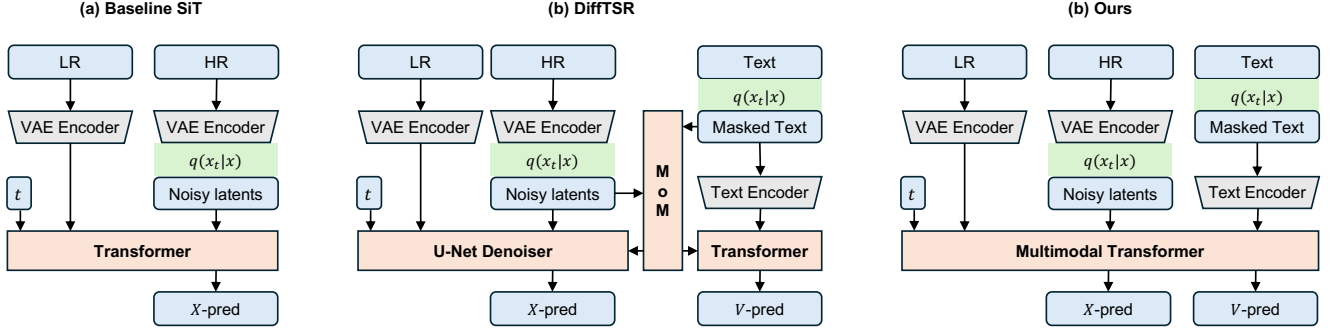


Figure 1. **A comparison of text super-resolution architectures.** Our proposed method unifies image generation and text recognition within a single model. (a) Baseline: Directly models the conditional distribution of high-resolution images from low-resolution inputs, without a text-based prior. (b) DiffTSR [44]: Independently models the image and text priors, subsequently fusing their representations using a Multi-modality Module (MoM). (c) Proposed Method: A unified multimodal transformer jointly optimizes for image generation and text recognition through two distinct but interconnected diffusion processes.

### 3.1. Preliminaries

Our model builds upon two key generative modeling paradigms: conditional flow matching for continuous data like images, and discrete diffusion for textual data.

#### 3.1.1. Conditional Flow Matching for Image Generation

Flow matching [17, 35] is a recent generative modeling paradigm that formulates sample generation as solving an ordinary differential equation (ODE) defined by a time-dependent velocity field. At inference, the goal is to generate a high-resolution image  $\mathbf{x}_0$  by solving an ODE over a time interval  $t \in [0, 1]$ . The process starts with a random noise sample  $\mathbf{x}_1$  drawn from a standard normal distribution,  $p_1(\mathbf{x}_1) = \mathcal{N}(0, I)$ . The ODE solver then integrates a learned conditional velocity field,  $\mathbf{v}_\theta(\mathbf{x}_t, t, \mathbf{c})$ , which guides the transformation from noise to an image. This velocity field is conditioned on external information  $\mathbf{c}$  (in our case, the low-resolution image and optionally text labels) and is parameterized by the image head of our multimodal network.

During training, the network  $\mathbf{v}_\theta$  is optimized to predict the velocity of a simple linear trajectory between a noise sample  $\mathbf{x}_1$  and a target data sample  $\mathbf{x}_0$ . The path is defined as

$$\mathbf{x}_t = (1 - t)\mathbf{x}_0 + t\mathbf{x}_1, \quad (1)$$

and its corresponding constant velocity is  $\mathbf{u}_t = \mathbf{x}_1 - \mathbf{x}_0$ . The CFM objective minimizes the discrepancy between the predicted velocity and this ground-truth velocity:

$$\mathcal{L}_{\text{CFM}} = \mathbb{E}_{t, q(\mathbf{x}_1), q(\mathbf{x}_0, \mathbf{c})} \|\mathbf{v}_\theta(\mathbf{x}_t, t, \mathbf{c}) - \mathbf{u}_t\|^2 \quad (2)$$

where  $t$  is sampled uniformly from  $[0, 1]$ ,  $q(\mathbf{x}_1) = \mathcal{N}(0, I)$  is the standard normal distribution, and  $q(\mathbf{x}_0, \mathbf{c})$  samples from the training dataset.

#### 3.1.2. Discrete Diffusion for Text Generation

For text generation, we require a diffusion process tailored for discrete data, where each token  $\mathbf{x}$  belongs to a finite vocabulary  $\mathcal{X} = \{1, \dots, N\}$ . While some methods apply diffusion in a continuous latent space [4, 5, 8, 12, 22], this can introduce mapping errors. We instead adopt a diffusion process that operates directly in the discrete token space, a paradigm that has shown strong empirical results [1, 21, 26, 30].

Our approach is based on a continuous-time Markov chain (CTMC) that defines a forward corruption process. Specifically, we use an absorbing-state diffusion process [21, 30, 32], where tokens in the original text sequence  $\mathbf{x}$  are progressively replaced by a special mask token  $\mathbf{m}$ . The marginal distribution of the corrupted text  $\mathbf{x}_t$  at time  $t$  is a categorical distribution conditioned on the original text  $\mathbf{x}$ :

$$q(\mathbf{x}_t | \mathbf{x}) = \text{Cat}[\mathbf{x}_t | \alpha_t \mathbf{x} + (1 - \alpha_t) \mathbf{m}], \quad (3)$$

where  $\text{Cat}(\cdot | \boldsymbol{\pi})$  is the categorical distribution with probabilities  $\boldsymbol{\pi}$ , and  $\alpha_t$  is a noise schedule.

The goal of the reverse process is to learn a denoising distribution  $p_\theta(\mathbf{x} | \mathbf{x}_t, t)$  that predicts the original clean text  $\mathbf{x}$  from its corrupted version  $\mathbf{x}_t$ . Following recent work [30, 32], we train the model by directly predicting the denoised variate. This leads to a simplified negative variational lower bound (NELBO) objective under the continuous-time limit:

$$L_{\text{NELBO}} = \mathbb{E}_{q(\mathbf{x}_t | \mathbf{x})} \left[ \int_0^1 \frac{-\alpha'_t}{1 - \alpha_t} \log p_\theta(\mathbf{x} | \mathbf{x}_t, t) dt \right]. \quad (4)$$

In practice, this integral is approximated using Monte-Carlo sampling. For the noise schedule, we follow Sahoo et al. [30] and use a simple log-linear schedule where  $\alpha_t = 1 - t$ .

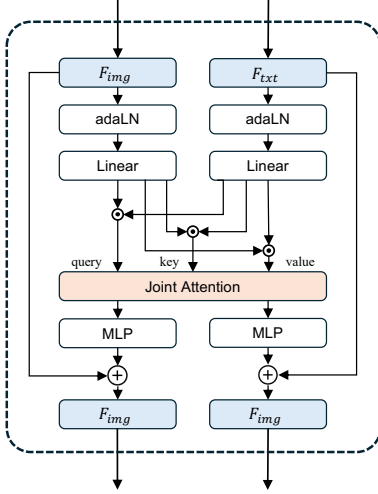


Figure 2. **Illustration of the joint attention mechanism.** Following the MM-DiT block design in SD3 [7], we incorporate a joint attention module that enables the image latent refinement and text reconstruction processes to operate in parallel.

### 3.2. Multimodal Transformer

To enable effective interaction between image and text modalities, we adopt a multimodal transformer architecture inspired by the MM-DiT block design from SD3 [7]. Unlike prior DiffTSR approaches [44], which rely on separate modality-specific models connected through an auxiliary communication module, our framework employs a unified transformer backbone. This unified design allows the model to dynamically attend to different modalities depending on the input, thereby supporting joint optimization of both the super-resolution task (LR-to-HR) and the recognition task (LR-to-text).

At the heart of this design is a joint attention mechanism [7]. As illustrated in Figure 2, latent tokens from the image and text diffusion processes are first processed independently. During the attention step, tokens from both modalities are concatenated to construct shared query, key, and value representations, which are passed through a single self-attention block. The resulting outputs are then split and routed back into their respective modality-specific streams. This mechanism achieves deep multimodal fusion, enabling visual features to directly guide text reconstruction and textual cues to inform image super-resolution at every layer of the network.

### 3.3. Training

To enable synchronized image and text generation at inference time, we optimize the continuous image process and the discrete text process jointly. Given a training triple  $(\mathbf{x}^{\text{hr}}, \mathbf{x}^{\text{lr}}, \mathbf{x}^{\text{txt}})$ , the HR image is encoded by a variational autoencoder [6] into the latent space used by the flow-

matching branch, while the text sequence is embedded into discrete tokens. For simplicity, we keep the notation  $\mathbf{x}^{\text{hr}}$  and  $\mathbf{x}^{\text{r}}$  for the corresponding latent variables in the equations below.

Let  $\mathbf{v}_\theta$  denote the image-velocity head and  $p_\theta$  denote the text-denoising head of the shared multimodal transformer. We sample

$$\mathbf{x}_t^{\text{hr}} = (1 - t)\mathbf{x}^{\text{hr}} + t\epsilon, \quad \epsilon \sim \mathcal{N}(0, I),$$

and corrupt the text with the absorbing process in Equation 3 to obtain  $\mathbf{x}_t^{\text{txt}}$ . The corresponding image target velocity is  $\mathbf{u}_t = \epsilon - \mathbf{x}^{\text{hr}}$ .

We first optimize modality-specific conditional objectives. For image generation, the model predicts the HR velocity conditioned on the LR image and the clean text:

$$\mathcal{L}_{\text{IMG}} = \mathbb{E}_{t,q} \|\mathbf{v}_\theta(\mathbf{x}_t^{\text{hr}}, t, \mathbf{c}^{\text{img}}) - \mathbf{u}_t\|_2^2, \quad (5)$$

where  $\mathbf{c}^{\text{img}} = \{\mathbf{x}^{\text{lr}}, \mathbf{x}^{\text{txt}}\}$ . For text prediction, the model reconstructs the clean text from corrupted tokens conditioned on the LR image and the clean HR image:

$$\mathcal{L}_{\text{TXT}} = \mathbb{E}_{q(\text{txt})} \left[ -\frac{1}{K} \sum_{i=1}^K \log p_\theta(\mathbf{x}_i^{\text{txt}} | \mathbf{x}_{t_i}^{\text{txt}}, t_i, \mathbf{c}^{\text{txt}}) \right], \quad (6)$$

where  $\mathbf{c}^{\text{txt}} = \{\mathbf{x}^{\text{lr}}, \mathbf{x}^{\text{hr}}\}$ . Following Li et al. [15], we approximate the continuous-time objective with antithetic sampling [11] over  $K$  timesteps  $t_i$  uniformly covering  $(\delta, 1]$ , where  $\delta$  is a small constant for numerical stability.

To strengthen joint modeling, we further corrupt both modalities with the same timestep and train the model to recover them simultaneously:

$$\mathcal{L}_{\text{Joint}} = \mathbb{E}_{t,q(\text{hr,lr,txt})} \left[ \|\mathbf{v}_\theta(\mathbf{x}_t^{\text{hr}}, t, \tilde{\mathbf{c}}^{\text{img}}) - \mathbf{u}_t\|_2^2 - \log p_\theta(\mathbf{x}_t^{\text{txt}} | \mathbf{x}_t^{\text{txt}}, t, \tilde{\mathbf{c}}^{\text{txt}}) \right], \quad (7)$$

where  $\tilde{\mathbf{c}}^{\text{img}} = \{\mathbf{x}^{\text{lr}}, \mathbf{x}_t^{\text{txt}}\}$  and  $\tilde{\mathbf{c}}^{\text{txt}} = \{\mathbf{x}^{\text{lr}}, \mathbf{x}_t^{\text{hr}}\}$ . The overall training objective is

$$\mathcal{L}_{\text{Overall}} = \mathcal{L}_{\text{IMG}} + \mathcal{L}_{\text{TXT}} + \mathcal{L}_{\text{Joint}}. \quad (8)$$

### 3.4. Model-Guided Training via Classifier-Free Guidance

To improve sample quality and controllability at inference time, we incorporate model guidance (MG) directly into training, following Tang et al. [34]. We apply this idea to the image-flow target in Equation 2. Let  $\mathbf{v}_\theta^{\text{ema}}(\mathbf{x}_t, t, \mathbf{c})$  be the conditioned velocity predicted by the EMA teacher model and  $\mathbf{v}_\theta^{\text{ema}}(\mathbf{x}_t, t, \emptyset)$  be the corresponding unconditional prediction. The flow-matching objective is then reformulated as

$$\mathcal{L}_{\text{CFM-MG}} = \mathbb{E}_{t,q(\mathbf{x}_0),q(\mathbf{x}_1,\mathbf{c})} \|\mathbf{v}_\theta(\mathbf{x}_t, t, \mathbf{c}) - \mathbf{u}'_t\|_2^2 \quad (9)$$

where the rectified target  $\mathbf{u}'_t$  is defined as:

$$\mathbf{u}'_t(\mathbf{x}_t, t, \mathbf{c}) = \mathbf{u}_t + w \cdot (\text{sg}(\mathbf{v}_\theta^{\text{ema}}(\mathbf{x}_t, t, \mathbf{c})) - \mathbf{v}_\theta^{\text{ema}}(\mathbf{x}_t, t, \emptyset)), \quad (10)$$

where  $w$  denotes the guidance scale factor and  $\text{sg}(\cdot)$  is the stop-gradient operator. Using the EMA teacher stabilizes the target prediction throughout training. During optimization, the condition vector  $\mathbf{c}$  is randomly replaced with  $\emptyset$  with probability  $\psi$  so that the network learns both conditional and unconditional predictions.

Applying this rectified target to the image-only and joint image losses gives

$$\begin{aligned} \mathcal{L}_{\text{IMG-MG}} &= \mathbb{E}_{t, q(\text{img})} \left\| \mathbf{v}_\theta(\mathbf{x}_t^{\text{hr}}, t, \mathbf{c}^{\text{img}}) - \mathbf{u}'_t(\mathbf{x}_t^{\text{hr}}, t, \mathbf{c}^{\text{img}}) \right\|_2^2, \\ \mathcal{L}_{\text{Joint-MG}} &= \mathbb{E}_{t, q(\text{img, txt})} \left[ \left\| \mathbf{v}_\theta(\mathbf{x}_t^{\text{hr}}, t, \tilde{\mathbf{c}}^{\text{img}}) - \mathbf{u}'_t(\mathbf{x}_t^{\text{hr}}, t, \tilde{\mathbf{c}}^{\text{img}}) \right\|_2^2 \right. \\ &\quad \left. - \log p_\theta(\mathbf{x}^{\text{txt}} | \mathbf{x}_t^{\text{txt}}, t, \tilde{\mathbf{c}}^{\text{txt}}) \right]. \end{aligned} \quad (11)$$

Our final training objective is then defined as:

$$\mathcal{L}_{\text{Overall}} = \mathcal{L}_{\text{IMG-MG}} + \mathcal{L}_{\text{TXT}} + \mathcal{L}_{\text{Joint-MG}}. \quad (12)$$

### 3.5. Joint inference

At inference time, given a low-resolution image  $\mathbf{x}^{\text{lr}}$ , we initialize the image branch from Gaussian noise  $\mathbf{x}_1^{\text{hr}}$  and the text branch from a fully masked sequence  $\mathbf{x}_1^{\text{txt}}$ . The shared transformer then updates both modalities synchronously. For a step from  $t$  to  $s$  ( $0 < s < t < 1$ ), the model predicts

$$\hat{\mathbf{u}}_t = \mathbf{v}_\theta(\mathbf{x}_t^{\text{hr}}, t, \{\mathbf{x}^{\text{lr}}, \mathbf{x}_t^{\text{txt}}\}), \quad (13)$$

$$\mathbf{p}_t = p_\theta(\cdot | \mathbf{x}_t^{\text{txt}}, t, \{\mathbf{x}^{\text{lr}}, \mathbf{x}_t^{\text{hr}}\}). \quad (14)$$

The image latent is updated with an Euler step,

$$\mathbf{x}_s^{\text{hr}} = \mathbf{x}_t^{\text{hr}} - (t - s)\hat{\mathbf{u}}_t, \quad (15)$$

while the text latent is updated by the reverse absorbing-state transition parameterized by  $\mathbf{p}_t$ , with only masked positions being resampled and already generated tokens kept fixed. After obtaining the final image latent  $\mathbf{x}_0^{\text{hr}}$ , we decode it back to RGB space using the VAE decoder. Detailed pseudocode for training and sampling is provided in Appendix A.4.

## 4. Experiments

### 4.1. Experimental Setup

**Datasets.** We evaluate the effectiveness of our method on two benchmarks. First, we construct a Chinese scene text super-resolution dataset, denoted as **CTR-TSR**. Following DiffTSR [44], we create training and testing splits

from CTR [41]; detailed construction procedures (filtering, canonical HR resizing, and blind degradation) are provided in Appendix A.2. Because the exact DiffTSR split is unavailable, we re-implemented the preprocessing pipeline per their description to ensure comparability. Second, we evaluate on the **RealCE** benchmark [25], which contains real-world Chinese text images. In practice, adapting the full benchmark to paired line-level STISR is difficult because many samples exhibit partial annotations, inaccurate localization, or severe LR–HR misalignment. We therefore report paired metrics on a curated subset of 300 samples with clean and well-aligned LR–HR pairs. These RealCE results should be interpreted under this explicit protocol rather than as a claim of full-benchmark superiority.

**Evaluation Metrics.** For both CTR-TSR and RealCE, we report PSNR ( $\uparrow$ ), LPIPS ( $\downarrow$ ), FID ( $\downarrow$ ), and two text fidelity metrics: ACC ( $\uparrow$ ) and NED ( $\uparrow$ ) [44]. ACC is the exact-match recognition accuracy (word-level); NED measures character level similarity by normalizing the Levenshtein distance [44]. To avoid evaluator drift, we use a fixed pre-trained OCR recognizer (TransOCR from CTR [41]) for all methods unless otherwise noted; computation details for the text metric are in Appendix A.7.

**Degradation and Resolutions.** Unless specified, HR images are resized to  $128 \times 512$  (text-line layout preserved). LR images are synthesized by a blind, stochastic pipeline (blur + noise + compression + downsampling, with random ordering/magnitudes) adapted from BSRGAN [43] and Real-ESRGAN [38]; full recipe and randomization ranges are summarized in Appendix A.2.

**Training Configuration.** Our model is implemented in PyTorch and trained on  $4 \times \text{NVIDIA A100 (40 GB)}$  GPUs. We use AdamW [20] with learning rate  $1 \times 10^{-4}$ , cosine decay, and weight decay 0.05. For CTR-TSR, we train for 700k iterations with batch size 32 (global). By default, we adopt  $K = 8$  discrete-text timesteps for antithetic sampling in the text diffusion loss and a 4-step ODE sampler for joint inference unless otherwise stated. Unless noted otherwise, we set the guidance scale factor  $w$  in Equation 10 to 1.0, which provides the best overall trade-off in Table 4. More experiment details are provided in Appendix A.3. Code, dataset construction scripts, and pretrained checkpoints will be released. **Baselines.** We compare with general SR methods (ESRGAN [37], MSRResNet [42], SwinIR [16], SRFormer [47]) and text-specific approaches (MARCONet [13], MARCONet++ [14], DiffTSR [44]). For MARCONet/MARCONet++, we use official checkpoints due to their tailored synthetic pipelines; DiffTSR is also evaluated with the official checkpoint on our test splits. Since these text-specific baselines are not retrained under a fully matched degradation pipeline, the comparison should be read as a reference comparison under a unified evaluation protocol rather than a perfectly controlled retraining study.

Table 1. Quantitative comparison on the synthetic CTR-TSR. Best in bold.

Method	$\times 2$					$\times 4$				
	PSNR $\uparrow$	LPIPS $\downarrow$	FID $\downarrow$	ACC $\uparrow$	NED $\uparrow$	PSNR $\uparrow$	LPIPS $\downarrow$	FID $\downarrow$	ACC $\uparrow$	NED $\uparrow$
ESRGAN [37]	24.09	0.3046	15.06	67.08%	83.79%	22.18	0.3986	18.25	43.69%	62.15%
MSRResNet [42]	28.03	0.3030	30.47	68.94%	85.37%	24.52	0.4029	50.60	49.04%	67.96%
SwinIR [16]	28.39	0.2983	31.54	70.01%	86.10%	24.73	0.3957	50.89	50.09%	68.93%
SRFormer [47]	<b>28.89</b>	0.2829	26.93	70.93%	86.91%	<b>25.05</b>	0.3801	46.23	51.83%	70.70%
MARCONet [13]	23.14	0.4518	88.06	57.93%	76.43%	25.05	0.3801	46.23	51.83%	70.70%
DiffTSR [44]	23.21	0.3304	18.57	63.51%	80.99%	20.62	0.3952	22.24	44.87%	63.20%
MARCONet++ [14]	24.02	0.4281	64.27	59.34%	77.49%	22.06	0.5072	86.18	39.92%	58.30%
<b>DualTSR (Ours)</b>	22.43	<b>0.2682</b>	<b>8.73</b>	<b>73.23%</b>	<b>88.50%</b>	20.54	<b>0.3292</b>	<b>16.42</b>	<b>57.65%</b>	<b>76.64%</b>

Table 2. Quantitative comparison on RealCE. Best in bold.

Method	$\times 2$					$\times 4$				
	PSNR $\uparrow$	LPIPS $\downarrow$	FID $\downarrow$	ACC $\uparrow$	NED $\uparrow$	PSNR $\uparrow$	LPIPS $\downarrow$	FID $\downarrow$	ACC $\uparrow$	NED $\uparrow$
ESRGAN [37]	20.08	0.3833	103.50	58.80%	86.30%	19.97	0.3721	87.18	58.50%	87.65%
MSRResNet [42]	19.25	<b>0.3033</b>	43.82	62.80%	89.08%	19.28	0.3590	60.81	58.00%	86.87%
SwinIR [16]	20.24	0.3810	87.98	59.30%	86.44%	20.23	0.3271	56.77	62.10%	87.55%
SRFormer [47]	<b>20.85</b>	0.3081	50.81	62.90%	89.47%	20.29	0.3732	83.47	57.50%	85.79%
MARCONet [13]	18.93	0.4144	87.54	60.58%	87.11%	<b>20.30</b>	0.3732	83.47	57.50%	85.79%
DiffTSR [44]	18.95	0.3179	38.13	62.60%	88.13%	18.09	0.3382	41.13	58.00%	84.44%
MARCONet++ [14]	19.38	0.3839	75.47	61.20%	87.47%	19.48	0.3953	81.72	59.40%	87.76%
<b>DualTSR (Ours)</b>	18.94	0.3133	<b>35.95</b>	<b>63.80%</b>	<b>89.97%</b>	18.85	<b>0.3277</b>	<b>40.78</b>	<b>62.20%</b>	<b>88.49%</b>

## 4.2. Main Results

**Quantitative.** Tables 1 and 2 report performance on the synthetic CTR-TSR benchmark and the real-world RealCE benchmark [25]. On CTR-TSR, generic SR models (ESRGAN [37], MSRResNet [42], SwinIR [16], SRFormer [47]) show strong PSNR but achieve poor LPIPS/FID and low ACC/NED at both  $\times 2$  and  $\times 4$ , confirming that high-fidelity image reconstruction alone is insufficient for recovering structured text. MARCONet [13] and MARCONet++ [14] introduce text-aware supervision, yet their compositing-based training often disrupts scene consistency and limits perceptual performance. DiffTSR improves FID through its dual diffusion branches, but the separation of text and image pathways still leads to occasional semantic errors. On this synthetic benchmark, DualTSR achieves the strongest FID/LPIPS/ACC/NED values across both  $\times 2$  and  $\times 4$  settings, although PSNR remains lower than several reconstruction-oriented baselines. This pattern suggests that the unified multimodal transformer favors perceptual realism and text fidelity over pure pixel-wise similarity.

On the curated RealCE subset, the real-world degradations amplify the weaknesses of prior approaches: generic SR models preserve coarse textures but fail to reconstruct valid glyphs, while MARCONet [13], MARCONet++ [14], and DiffTSR show limited robustness beyond their syn-

thetic training assumptions. Under this protocol, DualTSR achieves the best ACC and NED at both scales together with competitive perceptual quality. Because prior works often evaluate different filtered subsets or unreleased samples on RealCE, we interpret these results as protocol-specific evidence of transfer to real imagery rather than a definitive ranking on the full benchmark.

**Qualitative.** Figure 3 and Figure 4 provide  $\times 4$  visual comparisons on the CTR-TSR and RealCE datasets. Generic SR models tend to oversmooth strokes or introduce structural distortions, reflecting their lack of text-awareness. Text-oriented baselines better preserve character shapes, but MARCONet [13] and MARCONet++ [14] often generate glyphs that appear stylistically inconsistent or artificially pasted onto the background, despite occasionally producing correct character identities. DiffTSR yields sharper characters, yet its dual-branch design can lead to semantically incorrect predictions. In contrast, DualTSR more often recovers the correct textual content while preserving local appearance cues and keeping the text integrated with the surrounding scene. Failure cases still occur under severe corruption, especially when color or font cues are largely missing, in which case the model may prioritize legibility over exact style preservation. We provide more visual examples and additional  $\times 2$  qualitative results in Appendix A.8.

**Evaluation scope.** Our empirical claims are intentionally

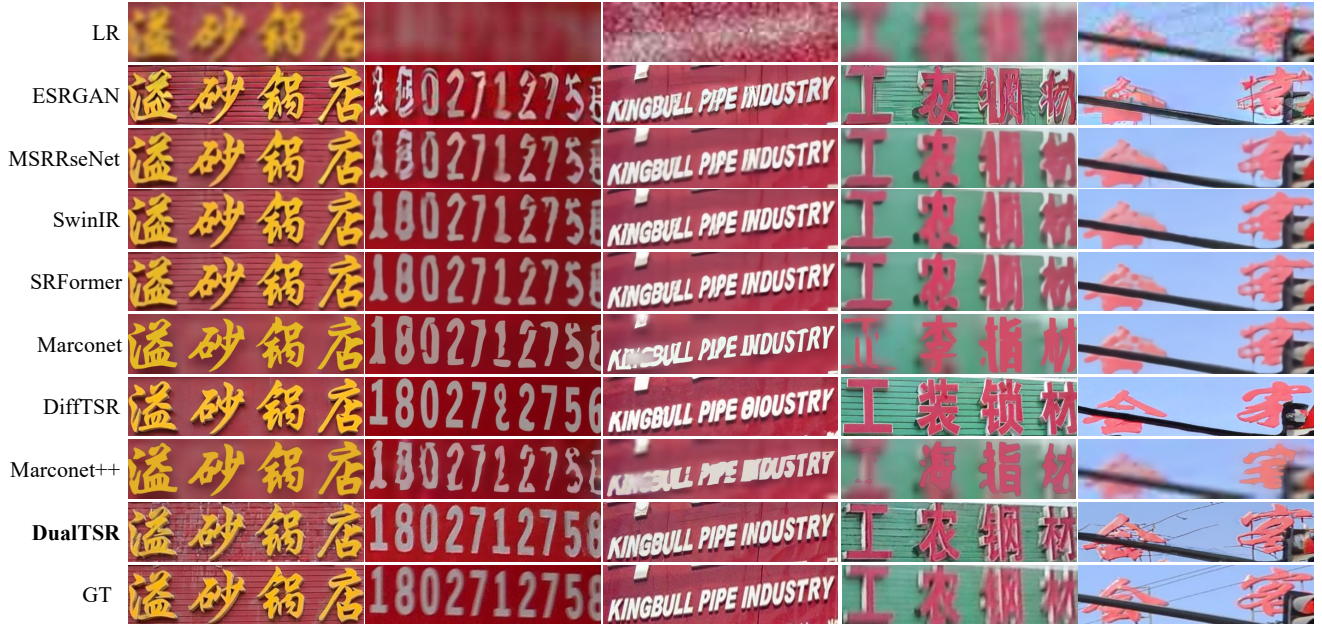


Figure 3. **Qualitative comparison for the synthetic dataset CTR-TSR-Test with different methods on  $\times 4$  scale.** The comparison methods include ESRGAN [37], MSRResNet [42], SwinIR [16], SRFormer [47], MARCONet [13], MARCONet++ [14], DiffTSR [44] and our method.

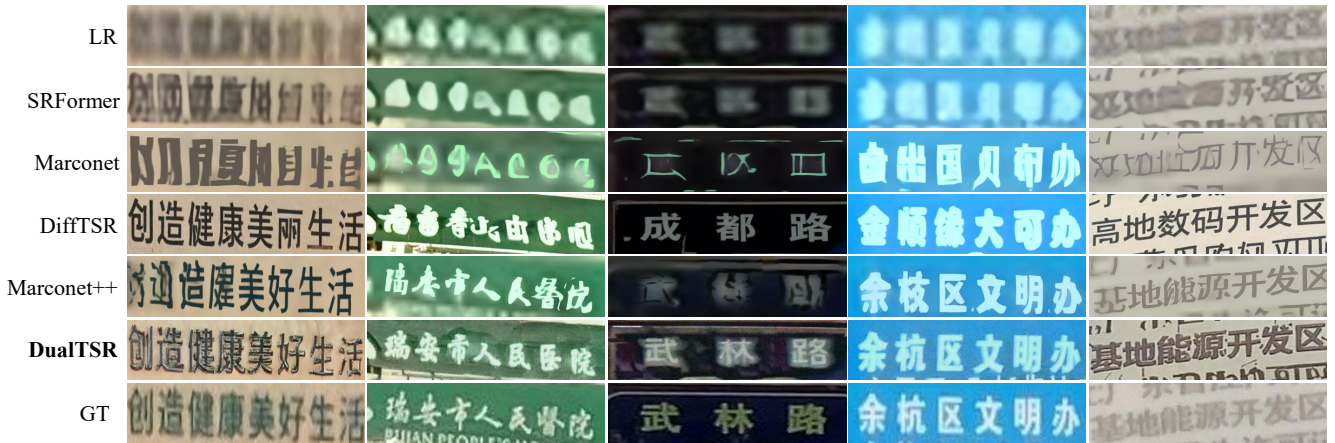


Figure 4. **Qualitative comparison for RealCE with different methods on  $\times 4$  scale.** The comparison methods include ESRGAN [37], MSRResNet [42], SwinIR [16], SRFormer [47], MARCONet [13], MARCONet++ [14], DiffTSR [44] and our method.

limited to the settings reported here. The paper evaluates Chinese STISR on CTR-TSR and on a curated RealCE protocol, and several text-specific baselines are compared through official checkpoints rather than matched retraining. Accordingly, we treat the main conclusion as evidence that a unified multimodal backbone can achieve strong text fidelity and perceptual quality without external OCR priors, rather than as a universal ranking over all STISR benchmarks and protocols.

### 4.3. Ablation Study

**Loss design ablation study.** Table 3 presents an ablation on our loss components. Starting with the baseline (a)  $\mathcal{L}_{\text{Joint-MG}}$ , the model already achieves strong results by jointly corrupting image and text with synchronized timesteps, yielding a balanced performance across both image quality (FID 13.73, LPIPS 0.3804) and text reconstruction (ACC 49.85%, NED 68.28%). Adding the discrete text diffusion loss (b)  $\mathcal{L}_{\text{Joint-MG}} + \mathcal{L}_{\text{TXT}}$  further improves the

Table 3. **Loss ablation study.** All models are trained for 300k iterations with a batch size of 128.

Setting	FID↓	PSNR↑	LPIPS↓	ACC↑	NED↑
(a) $\mathcal{L}_{\text{Joint-MG}}$	13.73	19.82	0.3804	49.85%	68.28%
(b) $\mathcal{L}_{\text{Joint-MG}} + \mathcal{L}_{\text{TXT}}$	13.39	19.79	0.3782	52.72%	72.17%
(c) $\mathcal{L}_{\text{Joint-MG}} + \mathcal{L}_{\text{TXT}} + \mathcal{L}_{\text{IMG-MG}}$	9.92	20.12	0.3550	53.71%	73.60%

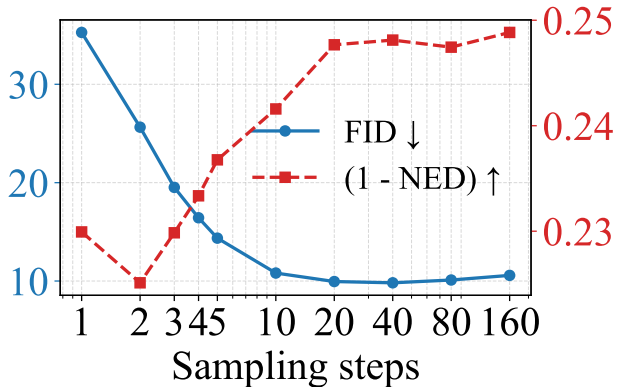


Figure 5. **Trade-off between perceptual quality and text fidelity across sampling steps.** FID improves with more sampling steps, reaching its best value around  $\sim 40$ , while NED worsens as text strokes become over-smoothed. We select 4 steps as a balanced operating point.

text metrics substantially (ACC +2.87, NED +3.89) while slightly reducing FID and LPIPS, indicating that explicit supervision on the text pathway stabilizes the shared Transformer and benefits both modalities.

Finally, incorporating the full image–text training objective (c)  $\mathcal{L}_{\text{Joint-MG}} + \mathcal{L}_{\text{TXT}} + \mathcal{L}_{\text{IMG-MG}}$  yields the best overall performance, improving FID from 13.39 to 9.92 and LPIPS from 0.3782 to 0.3550, while also boosting text accuracy to 53.71%. These gains show that the image MG loss complements the discrete text diffusion: image–level gradient signals regularize the latent Transformer and ensure that text reconstruction aligns with visually plausible high-resolution structures.

Overall, the ablation confirms the *Joint-MG* mechanism is essential for coupling the two modalities, while the additional image/text losses strengthen modality-specific reconstruction. The best results are achieved when all losses operate together, demonstrating that synchronized corruption paired with both continuous (image) and discrete (text) objectives leads to the most coherent multimodal generation.

**Effect of sampling steps.** Figure 5 illustrates the trade-off between perceptual realism and text fidelity as we vary the total number of sampling steps during inference. Increasing the number of steps generally improves FID, with the best perceptual quality achieved around 40 steps, reflecting more effective refinement of textures and global coherence.

In contrast, NED peaks at only 2 steps and degrades steadily as additional refinement is applied, indicating diminished character legibility. We hypothesize that with very few sampling steps, the model focuses on reconstructing coarse structures and high-contrast edges, which are crucial cues for recognizing fine-grained glyph shapes. As the total steps increase, the sampler devotes more iterations to enhancing textural realism and smoothing artifacts (see Fig. 6), but this refinement can inadvertently erode subtle, high-frequency stroke patterns—particularly problematic for dense scripts like Chinese where small details distinguish similar characters. Balancing these two factors, we adopt 4 sampling steps as our default setting, which provides a favorable compromise between natural image appearance and accurate text reconstruction.

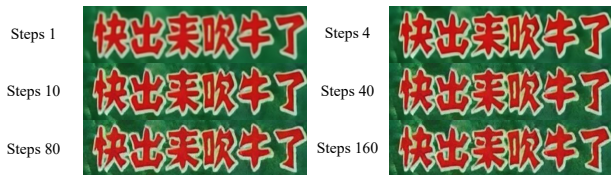


Figure 6. **Trade-off between perceptual quality and text fidelity across sampling steps.**

Table 4. Effect of CFG scale on FID and NED. Increasing CFG worsens FID and eventually harms NED.

CFG	1	1.45	2	4	6
FID↓	16.10	19.59	24.19	35.35	39.49
NED↑	76.66%	76.71%	75.95%	73.09%	72.20%

**Effect of CFG scale.** Table 4 shows the impact of classifier-free guidance (CFG) on our model. In contrast to typical image synthesis, where stronger guidance often improves perceptual sharpness [9], we find that increasing CFG consistently worsens FID, while NED remains nearly unchanged at 1.45 and then declines as guidance becomes stronger. Larger CFG values push the model toward overly confident predictions that deviate from the true data distribution, leading to unnatural textures and distorted character structures. We therefore use a CFG scale of 1.0, which offers the best overall trade-off. We hypothesize that strong guidance amplifies high-frequency hallucinations during sampling, which harms both visual naturalness and the fine-grained stroke patterns essential for accurate text reconstruction.

## 5. Conclusion

We presented *DualTSR*, a unified framework for text image super-resolution that integrates super-resolution and

text recognition within a single multimodal transformer. By jointly modeling continuous image generation and discrete text prediction, our method removes the reliance on external OCR priors and avoids the multi-stage, multi-model design of prior approaches such as DiffTSR. Experiments on CTR-TSR and on our curated RealCE evaluation protocol show that DualTSR provides strong perceptual quality and text fidelity within a single end-to-end model. At the same time, our current study is limited to Chinese benchmarks and checkpoint-based comparisons for some baselines; broader benchmark coverage and fully matched retraining remain important future work. We believe this unified perspective provides a promising direction for robust and scalable scene text restoration.

## References

- [1] Jacob Austin, Daniel D Johnson, Jonathan Ho, Daniel Tarlow, and Rianne Van Den Berg. Structured denoising diffusion models in discrete state-spaces. *NeurIPS*, 2021.
- [2] Jingye Chen, Bin Li, and Xiangyang Xue. Scene text telescope: Text-focused scene image super-resolution. In *CVPR*, 2021.
- [3] Jingye Chen, Haiyang Yu, Jianqi Ma, Bin Li, and Xiangyang Xue. Text gestalt: Stroke-aware scene text image super-resolution. In *AAAI*, 2022.
- [4] Ting Chen, Ruixiang Zhang, and Geoffrey Hinton. Analog bits: Generating discrete data using diffusion models with self-conditioning. *arXiv preprint arXiv:2208.04202*, 2022.
- [5] Sander Dieleman, Laurent Sartran, Arman Roshannai, Nikolay Savinov, Yaroslav Ganin, Pierre H Richemond, Arnaud Doucet, Robin Strudel, Chris Dyer, Conor Durkan, et al. Continuous diffusion for categorical data. *arXiv preprint arXiv:2211.15089*, 2022.
- [6] Patrick Esser, Robin Rombach, and Björn Ommer. Taming transformers for high-resolution image synthesis. In *CVPR*, 2021.
- [7] Patrick Esser, Sumith Kulal, Andreas Blattmann, Rahim Entezari, Jonas Müller, Harry Saini, Yam Levi, Dominik Lorenz, Axel Sauer, Frederic Boesel, Dustin Podell, Tim Dockhorn, Zion English, and Robin Rombach. Scaling rectified flow transformers for high-resolution image synthesis. In *ICML*, 2024.
- [8] Ishaan Gulrajani and Tatsunori B Hashimoto. Likelihood-based diffusion language models. *NeurIPS*, 2024.
- [9] Jonathan Ho and Tim Salimans. Classifier-free diffusion guidance. In *NeurIPS 2021 Workshop on Deep Generative Models and Downstream Applications*, 2021.
- [10] Jonathan Ho, Ajay Jain, and Pieter Abbeel. Denoising diffusion probabilistic models. *NeurIPS*, 2020.
- [11] Diederik Kingma, Tim Salimans, Ben Poole, and Jonathan Ho. Variational diffusion models. In *NeurIPS*, 2021.
- [12] Xiang Li, John Thackstun, Ishaan Gulrajani, Percy S Liang, and Tatsunori B Hashimoto. Diffusion-lm improves controllable text generation. *NeurIPS*, 2022.
- [13] Xiaoming Li, Wangmeng Zuo, and Chen Change Loy. Learning generative structure prior for blind text image super-resolution. In *CVPR*, 2023.
- [14] Xiaoming Li, Wangmeng Zuo, and Chen Change Loy. Enhanced generative structure prior for chinese text image super-resolution. *TPAMI*, 2025.
- [15] Zijie Li, Henry Li, Yichun Shi, Amir Barati Farimani, Yuval Kluger, Linjie Yang, and Peng Wang. Dual diffusion for unified image generation and understanding. In *CVPR*, 2025.
- [16] Jingyun Liang, Jiezhong Cao, Guolei Sun, Kai Zhang, Luc Van Gool, and Radu Timofte. Swinir: Image restoration using swin transformer. In *ICCV*, 2021.
- [17] Yaron Lipman, Ricky T. Q. Chen, Heli Ben-Hamu, Maximilian Nickel, and Matthew Le. Flow matching for generative modeling. In *ICLR*, 2023.
- [18] Baolin Liu, Zongyuan Yang, Pengfei Wang, Junjie Zhou, Ziqi Liu, Ziyi Song, Yan Liu, and Yongping Xiong. Textdiff: Mask-guided residual diffusion models for scene text image super-resolution. *arXiv preprint arXiv:2308.06743*, 2023.
- [19] Baolin Liu, Zongyuan Yang, Chinwai Chiu, and Yongping Xiong. Textdiff: Enhancing scene text image super-resolution with mask-guided residual diffusion models. *PR*, 2025.
- [20] Ilya Loshchilov and Frank Hutter. Decoupled weight decay regularization. In *ICLR*, 2019.
- [21] Aaron Lou, Chenlin Meng, and Stefano Ermon. Discrete diffusion language modeling by estimating the ratios of the data distribution. *arXiv preprint arXiv:2310.16834*, 2023.
- [22] Justin Lovelace, Varsha Kishore, Chao Wan, Eliot Shekhtman, and Kilian Q Weinberger. Latent diffusion for language generation. *NeurIPS*, 2024.
- [23] Jianqi Ma, Zhetong Liang, and Lei Zhang. A text attention network for spatial deformation robust scene text image super-resolution. In *CVPR*, 2022.
- [24] Jianqi Ma, Shi Guo, and Lei Zhang. Text prior guided scene text image super-resolution. *TIP*, 2023.
- [25] Jianqi Ma, Zhetong Liang, Wangmeng Xiang, Xi Yang, and Lei Zhang. A benchmark for chinese-english scene text image super-resolution. In *ICCV*, 2023.
- [26] Chenlin Meng, Kristy Choi, Jiaming Song, and Stefano Ermon. Concrete score matching: Generalized score matching for discrete data. *NeurIPS*, 2022.
- [27] Brian B Moser, Arundhati S Shanbhag, Federico Raue, Stanislav Frolov, Sebastian Palacio, and Andreas Dengel. Diffusion models, image super-resolution, and everything: A survey. *TNNLS*, 2024.
- [28] Axi Niu, Trung X Pham, Kang Zhang, Jinqiu Sun, Yu Zhu, Qingsen Yan, In So Kweon, and Yanning Zhang. Acldmsr: Accelerated conditional diffusion models for single image super-resolution. *TBC*, 2024.
- [29] Chihiro Noguchi, Shun Fukuda, and Masao Yamanaka. Scene text image super-resolution based on text-conditional diffusion models. In *WACV*, 2024.
- [30] Subham Sekhar Sahoo, Marianne Arriola, Aaron Gokaslan, Edgar Mariano Marroquin, Alexander M Rush, Yair Schiff, Justin T Chiu, and Volodymyr Kuleshov. Simple and effective masked diffusion language models. In *NeurIPS*, 2024.

- [31] Shuyao Shang, Zhengyang Shan, Guangxing Liu, LunQian Wang, XingHua Wang, Zekai Zhang, and Jinglin Zhang. Resdiff: Combining cnn and diffusion model for image super-resolution. In *AAAI*, 2024.
- [32] Jiaxin Shi, Kehang Han, Zhe Wang, Arnaud Doucet, and Michalis K. Titsias. Simplified and generalized masked diffusion for discrete data, 2024.
- [33] Jiaming Song, Chenlin Meng, and Stefano Ermon. Denoising diffusion implicit models. In *ICLR*, 2020.
- [34] Zhicong Tang, Jianmin Bao, Dong Chen, and Baining Guo. Diffusion models without classifier-free guidance. *arXiv preprint arXiv:2502.12154*, 2025.
- [35] Alexander Tong, Kilian FATRAS, Nikolay Malkin, Guillaume Hugué, Yanlei Zhang, Jarrid Rector-Brooks, Guy Wolf, and Yoshua Bengio. Improving and generalizing flow-based generative models with minibatch optimal transport. *Transactions on Machine Learning Research*, 2024.
- [36] Wenjia Wang, Enze Xie, Xuebo Liu, Wenhai Wang, Ding Liang, Chunhua Shen, and Xiang Bai. Scene text image super-resolution in the wild. In *ECCV*, 2020.
- [37] Xintao Wang, Ke Yu, Shixiang Wu, Jinjin Gu, Yihao Liu, Chao Dong, Yu Qiao, and Chen Change Loy. Esrgan: Enhanced super-resolution generative adversarial networks. In *ECCV Workshops*, 2018.
- [38] Xintao Wang, Liangbin Xie, Chao Dong, and Ying Shan. Real-esrgan: Training real-world blind super-resolution with pure synthetic data. In *ICCV*, 2021.
- [39] Baole Wei, Yuxuan Zhou, Liangcai Gao, and Zhi Tang. Glyphsr: A simple glyph-aware framework for scene text image super-resolution. In *AAAI*, 2025.
- [40] Gang Wu, Junjun Jiang, and Xianming Liu. A practical contrastive learning framework for single-image super-resolution. *TNNLS*, 2023.
- [41] Haiyang Yu, Jingye Chen, Bin Li, Jianqi Ma, Mengnan Guan, Xixi Xu, Xiaocong Wang, Shaobo Qu, and Xiangyang Xue. Benchmarking chinese text recognition: Datasets, baselines, and an empirical study. *arXiv preprint arXiv:2112.15093*, 2021.
- [42] Kai Zhang, Shuhang Gu, Radu Timofte, Zheng Hui, Xiumei Wang, Xinbo Gao, Dongliang Xiong, Shuai Liu, Ruipeng Gang, Nan Nan, Chenghua Li, Xueyi Zou, Ning Kang, Zhan Wang, Hang Xu, Chaofeng Wang, Zheng Li, Linlin Wang, Jun Shi, Wenyu Sun, Zhiqiang Lang, Jiangtao Nie, Wei Wei, Lei Zhang, Yazhe Niu, Peijin Zhuo, Xiangzhen Kong, Long Sun, and Wenhao Wang. Aim 2019 challenge on constrained super-resolution: Methods and results. In *ICCVW*, 2019.
- [43] Kai Zhang, Jingyun Liang, Luc Van Gool, and Radu Timofte. Designing a practical degradation model for deep blind image super-resolution. In *ICCV*, 2021.
- [44] Yuzhe Zhang, Jiawei Zhang, Hao Li, Zhouxia Wang, Luwei Hou, Dongqing Zou, and Liheng Bian. Diffusion-based blind text image super-resolution. In *CVPR*, 2024.
- [45] Minyi Zhao, Miao Wang, Fan Bai, Bingjia Li, Jie Wang, and Shuigeng Zhou. C3-stsr: Scene text image super-resolution with triple clues. *arXiv preprint arXiv:2204.14044*, 2022.
- [46] Zuoyan Zhao, Hui Xue, Pengfei Fang, and Shipeng Zhu. Pean: A diffusion-based prior-enhanced attention network for scene text image super-resolution. In *ACM MM*, 2024.
- [47] Yupeng Zhou, Zhen Li, Chun-Le Guo, Song Bai, Ming-Ming Cheng, and Qibin Hou. Srformer: Permuted self-attention for single image super-resolution. In *ICCV*, 2023.
- [48] Yuxuan Zhou, Liangcai Gao, Zhi Tang, and Baole Wei. Recognition-guided diffusion model for scene text image super-resolution. In *ICASSP*, 2024.

# DualTSR: Unified Dual-Diffusion Transformer for Scene Text Image Super-Resolution

## A. Appendix

### A.1. Architectural Comparison

Beyond quantitative and qualitative performance, our method also differs from prior diffusion-based STISR systems at the architectural level. DiffTSR [44] adopts a multi-stage pipeline composed of separate image and text diffusion branches plus an additional fusion module. Such a design offers strong modeling flexibility, but it also introduces more moving parts during training and evaluation.

In contrast, our framework unifies text recognition and image super-resolution within a single multimodal transformer and optimizes both branches end to end. Table 5 therefore summarizes structural differences in the training framework rather than measured runtime or memory costs. The key point is that DualTSR reduces the number of independently trained components while retaining joint image-text modeling.

Table 5. Comparison of training framework. Our framework consolidates text recognition and super-resolution into a single, end-to-end module, whereas DiffTSR [44] requires a multi-stage pipeline with multiple components and auxiliary models.

Feature	DiffTSR	Ours
<b>Training Stages</b>	3-stage training	End-to-end training
<b>Core Components</b>	3 (IDM, TDM, MoM)	1 (Multimodal Transformer)
<b>Auxiliary Models</b>	Pre-trained VAE + text recognizer	Pre-trained VAE

### A.2. CTR-TSR dataset construction

We build the **CTR-TSR** dataset from the CTR [41] corpus following the preprocessing and synthesis procedure described in DiffTSR [44]. In brief, the construction pipeline is:

1. **Source images.** Start from the scene part of CTR dataset [41] as the pool of high-quality HR text line images.
2. **Filtering and selection.** Retain only HR images that satisfy all of the following criteria:
  - resolution (longer side)  $\geq 64$  pixels;
  - width-to-height ratio  $> 2$  (to focus on text line images);
  - length of text annotation  $\leq 24$  characters.

After filtering and resizing (next step), this yields 64139 HR images which we denote CTR-TSR-Train.

3. **HR normalization.** Resize each selected HR image to a canonical HR size of  $128 \times 512$  for training (preserving the overall layout of text lines).
4. **LR synthesis (degradation).** We generate LR images using a blind, high-complexity degradation pipeline inspired by BSRGAN [43] and Real-ESRGAN [38]. During training, one of the two degradation strategies is randomly selected with equal probability ( $p = 0.5$ ) for each sample, and the corresponding LR image is synthesized online.
5. **Synthetic test set.** For the synthetic evaluation set (CTR-TSR-Test) we select images from the scene CTR test split, apply the same filtering/resizing and the same degradation pipeline as above. The resulting CTR-TSR-Test contains 8690 LR-HR pairs.

All synthesized LR images used for training and synthetic testing are generated with the same stochastic degradation pipeline so that training and evaluation are comparable across methods.

### A.3. Additional experiment details

The quantitative results in Tables 1 and 2 use CFG = 1.0 and 4 sampling steps. The qualitative results in Figures 3 and 4 use CFG = 1.0 and 160 sampling steps.

### A.4. Training and Sampling Pseudocode

Here, we provide pseudocode for the DualTSR training process in Algorithm 1 and the inference process in Algorithm 2.

```

1 def train_step(model, model_ema, optimizer, batch, w=1.0, psi=0.1):
2     x_hr, x_lr, text = batch # Unpack data batch
3
4     # 1. Image-Only Guided Loss (Flow Matching + Model Guidance)
5     t = torch.rand(x_hr.shape[0])
6     x_l = torch.randn_like(x_hr) # Sample Noise
7     x_t = (1 - t) * x_hr + t * x_l # Linear Interpolation
8
9     # Calculate Guidance Target using EMA Teacher
10    with torch.no_grad():
11        out_cond = model_ema(x_t, t, cond={'img': x_lr, 'txt': text})
12        out_unc = model_ema(x_t, t, cond={'img': x_lr, 'txt': None})
13
14        # Target = Base_Velocity + w * (Cond_Pred - Uncond_Pred)
15        u_target = (x_l - x_hr) + w * (out_cond - out_unc)
16
17    # Student Prediction (with CFG dropout)
18    cond = {'img': x_lr, 'txt': text} if rand() > psi else {'img': x_lr, 'txt': None}
19    u_pred = model(x_t, t, cond)
20    loss_img = F.mse_loss(u_pred, u_target)
21
22    # 2. Text-Only Loss (Masked Generative Training)
23    t_txt = sample_timesteps()
24    text_masked = mask_tokens(text, ratio=1-t_txt)
25
26    logits_txt = model(text_masked, t_txt, cond={'img': x_hr}, mode='text')
27    loss_txt = F.cross_entropy(logits_txt, text) / t_txt
28
29    # 3. Joint Guided Loss (Simultaneous Generation)
30    t_j = torch.rand(x_hr.shape[0])
31    x_t_j = (1 - t_j) * x_hr + t_j * x_l
32    txt_t_j = mask_tokens(text, ratio=1-t_j)
33
34    with torch.no_grad():
35        # Joint guidance targets from EMA
36        c_j = {'txt_in': txt_t_j, 'lr': x_lr}
37        u_j_c = model_ema(x_t_j, t_j, c_j)
38        u_j_u = model_ema(x_t_j, t_j, {'txt_in': None, 'lr': x_lr})
39        u_target_j = (x_l - x_hr) + w * (u_j_c - u_j_u)
40
41    c_stud = c_j if rand() > psi else {'txt_in': None, 'lr': x_lr}
42    u_pred_j, logits_j = model(x_t_j, t_j, c_stud, mode='joint')
43    loss_joint = F.mse_loss(u_pred_j, u_target_j) + F.cross_entropy(logits_j, text)
44
45    # Optimization Step
46    loss = loss_img + loss_txt.mean() + loss_joint
47    loss.backward()
48    optimizer.step()
49    update_ema(model, model_ema)

```

Algorithm 1. PyTorch-style pseudocode for the proposed DualTSR training strategy. We utilize an EMA teacher model to provide guidance targets for the flow matching objective.

## A.5. Reproduction Details for Different Methods

For MSRResNet [42] and ESRGAN [37], we use the BasicSR<sup>1</sup> codebase to train the models on our CTR-TSR-Train dataset with the default settings. For SRFormer [47], we use the official code and training settings from the original paper. For DiffTSR [44], we use the official checkpoint for direct inference on our test splits. For MARCONet [13] and MARCONet++ [14], we use the publicly available checkpoints because these models rely on carefully designed data-synthesis pipelines and are intended to generalize to real-world scenarios. Since DiffTSR, MARCONet, and MARCONet++ are not retrained under an identical degradation pipeline, these comparisons should be interpreted as reference comparisons under

<sup>1</sup><https://github.com/XPixelGroup/BasicSR/tree/master>

```

1 def joint_inference(model, x_lr, steps=50, seq_len=25):
2     # 1. Initialization
3     bs = x_lr.shape[0]
4     x = torch.randn_like(x_lr)           # Image Latent (t=1)
5     text = torch.full((bs, seq_len), MASK_TOKEN) # Text Latent (All Masked)
6
7     # Time schedule from 1.0 down to 0.0
8     timesteps = torch.linspace(1.0, 0.0, steps + 1)
9     dt = 1.0 / steps
10
11    # 2. Generation Loop
12    for k in range(steps):
13        t = timesteps[k]
14        s = timesteps[k+1] # Next timestep
15
16        # Predict Velocity and Text Logits
17        u_pred, logits_txt = model(x, t, text, cond=x_lr)
18
19        # --- A. Image Update (Euler ODE Step) ---
20        # Reverse the flow: subtract velocity to go from Noise -> Data
21        x = x - dt * u_pred
22
23        # --- B. Text Update (Reverse Discrete Diffusion) ---
24        # Determine probability to unmask at this step
25        alpha_t, alpha_s = 1 - t, 1 - s
26        prob_unmask = (alpha_s - alpha_t) / (1.0 - alpha_t + 1e-8)
27
28        # Sample candidate tokens from model prediction
29        probs = F.softmax(logits_txt, dim=-1)
30        candidates = torch.multinomial(probs.view(-1, probs.size(-1)), 1).view(bs, seq_len)
31
32        # Update Logic:
33        # If token is [MASK] AND random < prob_unmask -> Update with candidate
34        # Else -> Keep current state (either already generated or still [MASK])
35        is_masked = (text == MASK_TOKEN)
36        should_sample = torch.rand_like(text.float()) < prob_unmask
37
38        update_mask = is_masked & should_sample
39        text[update_mask] = candidates[update_mask]
40
41    return x, text

```

Algorithm 2. PyTorch-style inference algorithm. The image is generated via ODE flow integration, while the text is generated via iterative unmasking (discrete diffusion) synchronized with the image generation steps.

a common evaluation protocol rather than as fully controlled retraining results. We observe that MARCONet++ requires detectable text in the LR image; when the model fails to detect text, inference raises an error. In such cases, we use the LR image directly as the model output. This issue is especially common in real-world samples whose text can barely be recognized.

## A.6. Protocol Note on RealCE

RealCE was originally released for real-world text image super-resolution, but paired metric evaluation is difficult when adapting it to line-level Chinese STISR because some samples contain partial annotations, inaccurate localization, or severe LR–HR misalignment. For this reason, we report paired metrics on a curated subset of 300 clean LR–HR pairs. This protocol improves measurement stability and reproducibility, but the resulting numbers should be understood as protocol-specific rather than as a full-benchmark ranking.

## A.7. Text-Related Metrics

**ACC (word accuracy / recognition accuracy).** ACC is the exact-match recognition accuracy: the fraction of test samples for which the predicted text sequence equals the ground-truth transcription. In all experiments in this paper, we use the pretrained TransOCR recognition model from [41] (as in DiffTISR) to obtain predictions used in ACC calculation. Higher

ACC indicates better preservation of textual content in the restored image.

**NED (Normalized Edit Distance).** NED quantifies character-level similarity by normalizing the Levenshtein (edit) distance between the predicted and ground-truth strings. For a single sample with ground truth  $g$  and prediction  $p$  we compute:

$$\text{NED}(p, g) = 1 - \frac{\text{ED}(p, g)}{\max(|g|, |p|)},$$

where  $\text{ED}(\cdot, \cdot)$  is the Levenshtein distance and  $|g|$ , and  $|p|$  is the length of the ground truth and prediction. We report the dataset mean NED; larger values indicate better (closer) recognition. In CTR-TSR evaluations ACC and NED are computed using the pretrained TransOCR recognizer, as in DiffTSR.

## A.8. More Qualitative examples

### A.8.1. On synthetic CTR-TSR

For the synthetic CTR-TSR test set, we provide additional  $\times 2$  results in Figures 7 and 8, and additional  $\times 4$  results in Figure 9.



Figure 7. **Visual comparison for the synthetic dataset CTR-TSR-Test with different methods on  $\times 2$  scale.** The comparison methods include ESRGAN [37], MSRResNet [42], SwinIR [16], SRFormer [47], MARCONet [13], MARCONet++ [14], DiffTSR [44] and our method.

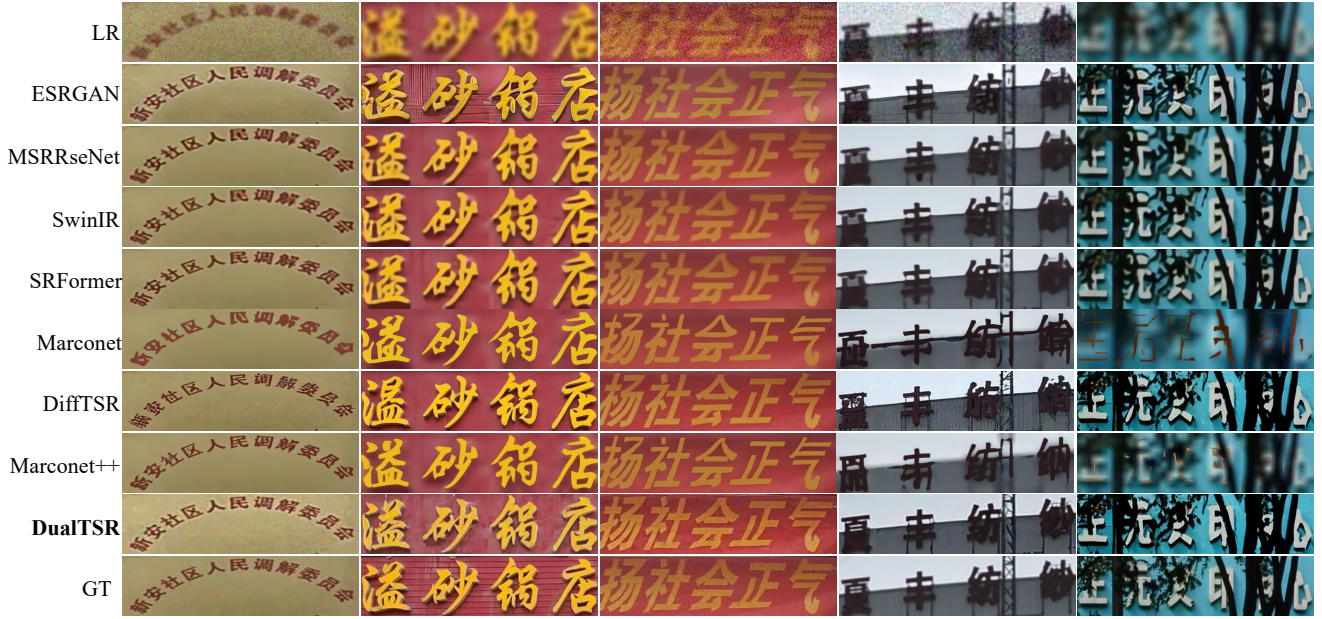


Figure 8. **Visual comparison for the synthetic dataset CTR-TSR-Test with different methods on  $\times 2$  scale.** The comparison methods include ESRGAN [37], MSRResNet [42], SwinIR [16], SRFormer [47], MARCONet [13], MARCONet++ [14], DiffTSR [44] and our method.



Figure 9. **Visual comparison for the synthetic dataset CTR-TSR-Test with different methods on  $\times 4$  scale.** The comparison methods include ESRGAN [37], MSRResNet [42], SwinIR [16], SRFormer [47], MARCONet [13], MARCONet++ [14], DiffTSR [44] and our method.

### A.8.2. On real-world dataset RealCE

For the real-world RealCE benchmark, we provide additional  $\times 2$  results in Figures 10 and 11, and additional  $\times 4$  results in Figures 12 and 13.

LR		承接大型婚宴、团队、会议	秀姿美容	汉庭集中隔离点	蔗糖,一杯60kcal
ESRGAN		承接大型婚宴、团队、会议	秀姿美容	汉庭集中隔离点	蔗糖,一杯60kcal
MSRRseNet		承接大型婚宴、团队、会议	秀姿美容	汉庭集中隔离点	蔗糖,一杯60kcal
SwinIR		承接大型婚宴、团队、会议	秀姿美容	汉庭集中隔离点	蔗糖,一杯60kcal
SRFormer		承接大型婚宴、团队、会议	秀姿美容	汉庭集中隔离点	蔗糖,一杯60kcal
Marconet		承接大型婚宴、团队、会议	秀姿美容	汉庭集中固离点	蔗糖,一杯60kcal
DiffTSR		承接大型婚宴、团队、会议	秀姿美容	汉庭集中届离点	蔗糖,一杯60kcal
Marconet++		承接大型婚宴、团队、会议	秀姿美容	江超第中题离点	蔗糖,一杯60kcal
DualTSR		承接大型婚宴、团队、会议	秀姿美容	汉庭集中隔离点	蔗糖,一杯60kcal
GT		承接大型婚宴、团队、会议	秀姿美容	汉庭集中隔离点	蔗糖,一杯60kcal

Figure 10. **Visual comparison for the real-world dataset RealCE with different methods on  $\times 2$  scale.** The comparison methods include ESRGAN [37], MSRRseNet [42], SwinIR [16], SRFormer [47], MARCONet [13], MARCONet++ [14], DiffTSR [44] and our method.

LR		地址:瑞安市玉海街道青松路	东野圭吾作品 5	对重度污渍预处理效果更佳	请先收下这句感谢。
ESRGAN		地址:瑞安市玉海街道青松路	东野圭吾作品 5	对重度污渍预处理效果更佳	请先收下这句感谢。
MSRRseNet		地址:瑞安市玉海街道青松路	东野圭吾作品 5	对重度污渍预处理效果更佳	请先收下这句感谢。
SwinIR		地址:瑞安市玉海街道青松路	东野圭吾作品 5	对重度污渍预处理效果更佳	请先收下这句感谢。
SRFormer		地址:瑞安市玉海街道青松路	东野圭吾作品 5	对重度污渍预处理效果更佳	请先收下这句感谢。
Marconet		地址:瑞安市玉海街道青松路	东野圭吾作品 5	对重度污渍预处理效果更佳	请先收下这句感谢。
DiffTSR		地址:瑞安市玉海街道青松路	东野圭吾作品 5	对重度污渍预处理效果更佳	请先收下这句感谢。
Marconet++		地址:瑞安市玉海街道青松路	东野圭吾作品 5	对重度污渍预处理效果更佳	请先收下这句感谢。
DualTSR		地址:瑞安市玉海街道青松路	东野圭吾作品 52	对重度污渍预处理效果更佳	请先收下这句感谢。
GT		地址:瑞安市玉海街道青松路	东野圭吾作品 52	对重度污渍预处理效果更佳	请先收下这句感谢。

Figure 11. **Visual comparison for the real-world dataset RealCE with different methods on  $\times 2$  scale.** The comparison methods include ESRGAN [37], MSRRseNet [42], SwinIR [16], SRFormer [47], MARCONet [13], MARCONet++ [14], DiffTSR [44] and our method.



Figure 12. **Visual comparison for the real-world dataset RealCE with different methods on  $\times 4$  scale.** The comparison methods include ESRGAN [37], MSRResNet [42], SwinIR [16], SRFormer [47], MARCONet [13], MARCONet++ [14], DiffTSR [44] and our method.



Figure 13. **Visual comparison for the real-world dataset RealCE with different methods on  $\times 4$  scale.** The comparison methods include ESRGAN [37], MSRResNet [42], SwinIR [16], SRFormer [47], MARCONet [13], MARCONet++ [14], DiffTSR [44] and our method.